



Cite this: DOI: 10.1039/d0na00052c

A broadband ultraviolet light source using GaN quantum dots formed on hexagonal truncated pyramid structures†

Jong-Hoi Cho,^{‡a} Seung-Hyuk Lim,^{‡§a} Min-Ho Jang,^a Chulwon Lee,^a Hwan-Seop Yeo,^a Young Chul Sim,^a Je-Hyung Kim,^a Samuel Matta,^b Blandine Alloing,^b Mathieu Leroux,^b Seoung-Hwan Park,^c Julien Brault^b and Yong-Hoon Cho^{ID}*^a

Group III-nitride semiconductor-based ultraviolet (UV) light emitting diodes have been suggested as a substitute for conventional arc-lamps such as mercury, xenon and deuterium arc-lamps, since they are compact, efficient and have a long lifetime. However, in previously reported studies, group III-nitride UV light emitting diodes did not show a broad UV spectrum range as conventional arc-lamps, which restricts their application in fields such as medical therapy and UV spectrophotometry. Here, we propose GaN quantum dots (QDs) grown on different facets of hexagonal truncated pyramid structures formed on a conventional (0001) sapphire substrate. A hexagonal truncated GaN pyramid structure includes {10 $\bar{1}1$ } semipolar facets as well as a (0001) polar facet, which have intrinsically different piezoelectric fields and growth rates of GaN QDs. Consequently, we successfully demonstrated a plateau-like broadband UV spectrum ranging from ~400 nm (UV-A) to ~270 nm (UV-C) from the GaN QDs. In addition, at the top-edge of the truncated pyramid structure, a strain was locally suppressed compared to the center of the truncated pyramid structure. As a result, various emission wavelengths in the UV range were achieved from the GaN QDs grown on the sidewall, top-edge and top-center of hexagonal truncated pyramid structures, which ultimately provide a broadband UV spectrum with high efficiency.

Received 2nd December 2019
Accepted 10th February 2020

DOI: 10.1039/d0na00052c

rsc.li/nanoscale-advances

Introduction

Group III-nitride semiconductor-based ultraviolet (UV) light emitting diodes (LEDs) have received significant attention in recent years as a substitute for conventional arc-lamps such as mercury, xenon and deuterium arc-lamps.^{1–4} UV LEDs can be extensively used for numerous UV applications such as polymer curing, sterilization¹ and photolithography.^{2,3} In general, group III-nitride semiconductors have large defect density due to lattice mismatch and thermal expansion difference with respect to foreign substrates such as sapphire, SiC, Si, *etc.* In this respect, some research studies have focused on quantum dot (QD) based LEDs since the QDs enable strong carrier

localization,^{5,6} which prohibits carriers from being captured by defects. In addition, their emission wavelength can be manipulated *via* the quantum effect in QDs.^{7–9} Indeed, the emission wavelength of GaN QDs can be shorter than the GaN band-edge emission due to the quantum-confinement effect,⁹ but can also be longer due to the presence of an internal electric field and the consequent quantum confined Stark effect.^{9,10} As a result, the emission wavelength of GaN QDs grown on a (0001) polar sapphire substrate has remained in the UV-A range.¹¹ For deeper UV emission, GaN QDs grown on unconventional substrates with nonpolar or semipolar planes can be adopted, which have a negligible internal electric field. Although various methods for manipulating the emission wavelength have been suggested, previous studies have focused only on achieving a narrow UV emission spectrum. As a result, the emission spectrum range of UV LEDs is not as broad as that of conventional arc-lamps, and thus the need for achieving a solid-state based broadband UV light source still remains. Because of the spectral limitations of conventional UV LEDs, some applications such as UV spectrophotometry^{12,13} and photodynamic therapy in dermatology^{14,15} still require arc-lamps even though the arc-lamp system is impractical and inefficient due to their bulky system, heat generation and poor lifetime.

^aDepartment of Physics, KI for the NanoCentury, Korea Advanced Institute of Science and Technology (KAIST), Daejeon 34141, Republic of Korea. E-mail: yhc@kaist.ac.kr

^bUniversité Côte d'Azur, CNRS, CRHEA, 06560 Valbonne, France

^cDepartment of Electronics Engineering, Catholic University of Daegu, Kyeongsan 38430, Republic of Korea

† Electronic supplementary information (ESI) available. See DOI: 10.1039/d0na00052c

‡ These authors equally contributed.

§ Present address: R&D Investment Planning Team, Korea Institute of S&T Evaluation and Planning (KISTEP), Chungcheongbuk-do 27740, Republic of Korea.



Here, we propose a combination of GaN/AlGa_xN QDs grown on GaN-based hexagonal truncated pyramid structures for a solid-state broadband UV light source. In this structure, GaN QDs were used as active layers embedded in Al_xGa_{1-x}N ($x \sim 0.5$, nominal composition) matrix layers.^{16,17} Although a *c*-plane sapphire substrate was used, the GaN-based hexagonal truncated pyramid structures include (0001) polar and {10 $\bar{1}$ 1} semipolar facets, which have intrinsically different internal electric fields as well as growth rates depending on the facet.¹⁸ Therefore, the GaN QDs grown on different facets show various UV emission wavelengths and structural properties. In particular, the GaN QDs grown on the top-edge of the hexagonal truncated pyramid structures have locally suppressed strain, and have distinct properties from those at the top-center of these structures in spite of the same (0001) polar facet. Based on these unique properties, we successfully demonstrate a plateau-like broadband UV spectrum covering the wavelength range from ~ 400 nm (UV-A) to ~ 270 nm (UV-C) and expect to replace many arc-lamp-based applications.

Results and discussion

Fig. 1a–c show the fabrication process of the GaN QDs on GaN-based hexagonal truncated pyramid structures for the broadband UV light source device. To fabricate such a unique structure, we combined both a selective area growth technique¹⁸ by metal–organic chemical vapor deposition (MOCVD) and a 2D–3D growth mode transition, *i.e.* equivalent to the so-called Stranski–Krastanov (SK) growth technique, using molecular beam epitaxy (MBE). After a GaN template was first grown on a *c*-sapphire substrate by MOCVD, a SiN_x layer was deposited and hole patterns with 20 μ m diameter were fabricated by lithography and dry etching. The hexagonal truncated pyramid GaN structures were formed by a second MOCVD process. After

a nominal 175 nm AlN buffer layer was grown by MBE on the GaN truncated pyramid structures to avoid cracks, a nominal 810 nm-thick Al_xGa_{1-x}N ($x \sim 0.5$, nominal composition) layer was grown. Two layers containing GaN QDs, using a deposited GaN amount of six monolayers (*i.e.* with one monolayer corresponding approximately to 0.25 nm), were formed on these truncated pyramid structures by triggering a 2D–3D “SK type” growth mode transition¹⁹ separated by a 30 nm-thick Al_xGa_{1-x}N quantum barrier. In between these GaN QDs, a thin wetting layer of a few monolayers composed of GaN was formed, which is a typical signature of the 2D–3D morphological transition of the deposited GaN layer.¹⁶ By not capping the last QD layer, the geometric morphology of the GaN QDs can be investigated.

An overall tilted scanning electron microscopy (SEM) image of the sample after the MOCVD and MBE growth is shown in Fig. 1d. The truncated pyramid structure mainly consists of two types of facets, (0001) polar and {10 $\bar{1}$ 1} semipolar facets. Fig. 1e shows a cross-sectional schematic (location and direction indicated with the green box and the arrow in Fig. 1d) along the $\langle 1\bar{2}10 \rangle$ axis. A high angle annular dark field scanning transmission electron microscopy (HAADF STEM) image was taken at the boundary between the (0001) polar and {10 $\bar{1}$ 1} semipolar facets (the yellow square in Fig. 1e) as shown in Fig. 1f. With clear contrast, we confirmed that the AlN and Al_xGa_{1-x}N layers grown by MBE were successfully fabricated on the MOCVD-grown GaN structure. Two sets of QD layers were also observed in the magnified HAADF STEM image (Fig. 1g).

Fig. 2a shows the top-view SEM image of an entire single truncated pyramid structure. As shown in Fig. 2b, the GaN QDs grown on the (0001) polar facet (P-QDs) were densely formed on the surface. Interestingly, we found one or two rows of QDs within 200 nm width along the boundary line between the (0001) polar and {10 $\bar{1}$ 1} semipolar facets, which are spatially distinguished from the P-QDs. In other words, these QDs were

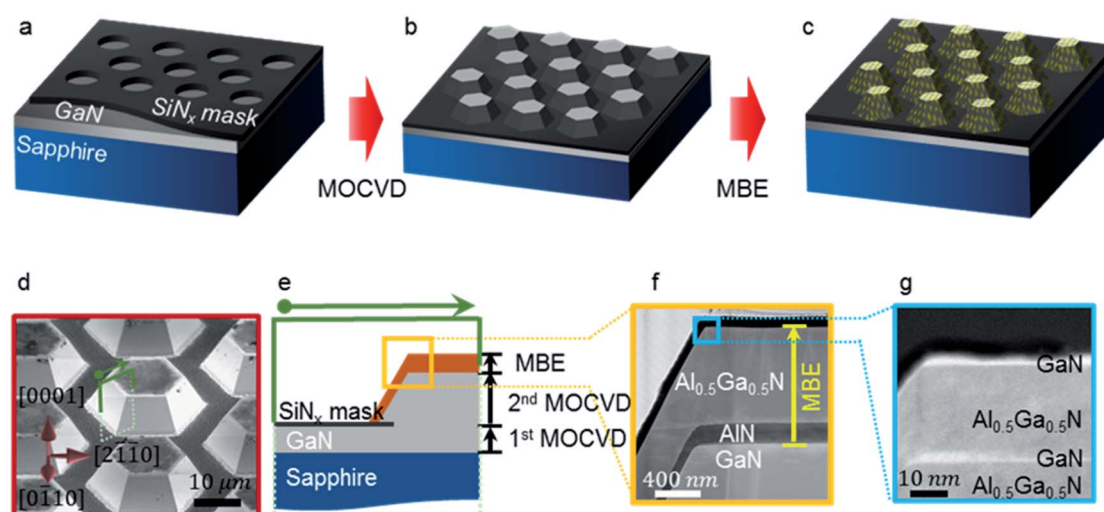


Fig. 1 Schematics of the fabrication process of GaN QDs on truncated pyramids. (a) Hole patterned SiN_x layer deposited on the 1st MOCVD-grown GaN template. (b) 2nd MOCVD growth: selective area growth for GaN truncated pyramids. (c) MBE growth: AlN/Al_xGa_{1-x}N/GaN QDs. (d) Bird's eye view SEM image of GaN QDs on truncated pyramid structures. (e) Cross-sectional schematic of GaN QDs on a truncated pyramid structure indicated with a green box and arrow in (d). (f) Cross-sectional HAADF STEM image of an MBE-grown region indicated with a yellow box in (e). (g) Magnified HAADF STEM image of the boundary between the (0001) polar and {10 $\bar{1}$ 1} semipolar facets indicated with a blue box in (f).



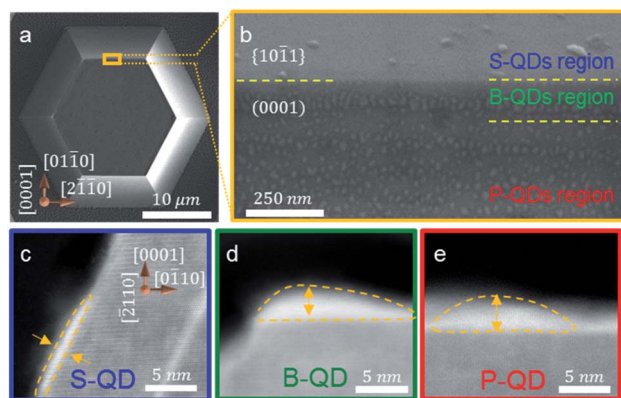


Fig. 2 (a) Top-view SEM image of a single truncated pyramid. (b) High-resolution SEM image of the boundary between (0001) polar and $\{10\bar{1}1\}$ semipolar facets. (c–e) HAADF STEM images of S-, B-, and P-QDs on the surface of the truncated pyramid, respectively.

formed along the boundary line, while the other P-QDs were randomly formed on the surface (see ESI Fig. S1†). Given this distinction, we named those QDs grown on the boundary region B-QDs. In the case of the QDs grown on the $\{10\bar{1}1\}$ semipolar facets (S-QDs), a few S-QDs have comparable size to that of the P-QDs. But, most of the S-QDs were too small to be clearly observed by SEM.

To clarify the morphological characteristics of the S-, B-, and P-QDs, HAADF STEM was conducted. Fig. 2c–e present the HAADF STEM images of single S-, B-, and P-QDs, respectively. The average heights of the S-, B- and P-QDs are 1.09 ± 0.25 nm, 2.57 ± 0.20 nm, and 2.91 ± 0.47 nm, respectively. Since the HAADF STEM sample was prepared using a focused ion beam along $[01\bar{1}0]$, dozens of S-QDs and P-QDs were checked to measure their heights but only two B-QDs were measured because of the tiny boundary region. The height of the S-QDs was approximately one-third smaller than that of B- and P-QDs because of the angled source flux during MBE. This height ratio corresponds to the thickness ratio of the AlN and $\text{Al}_x\text{Ga}_{1-x}\text{N}$ layers between the (0001) polar and $\{10\bar{1}1\}$ semipolar facets, which was about one-third (Fig. 1f).

We measured photoluminescence (PL) and PL excitation (PLE) spectra at 10 K as shown in Fig. 3. A plateau-like broadband UV emission ranging from UV-A to UV-C was observed as shown in Fig. 3a. When measuring the monochromatic cathodoluminescence (CL) images at 10 K, the emission regions of each wavelength could be spatially distinguished, as shown in Fig. 3b–f. The emission wavelengths of S-, B- and P-QDs revealed a blue-shift from the bulk GaN peak because of the quantum confinement effect.^{9,10} The emission wavelength of S-QDs was shorter than those of the B- and P-QDs due to the smaller height of S-QDs and the negligible built-in electric field of $\{10\bar{1}1\}$ semipolar facets.⁸

Interestingly, we found that the emission wavelength of B-QDs was clearly distinguished from those of P-QDs or S-QDs, as shown in Fig. 3e. The emission wavelength of B-QDs is shorter than that of P-QDs even though they were grown on the same (0001) polar facet. Furthermore, the CL emission from the

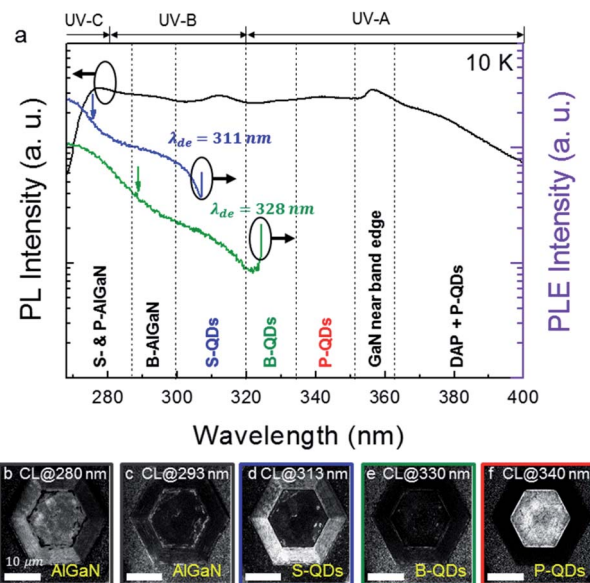


Fig. 3 (a) PL and PLE spectra at 10 K. The black line shows the broadband UV emission spectrum. Blue and green lines indicate the PLE intensity of S- and B-QDs, respectively. DAP stands for donor-to-acceptor pair. (b–f) Low-temperature (10 K) monochromatic CL images of a single truncated pyramid measured at 280 nm, 293 nm, 313 nm, 330 nm, and 340 nm, respectively (scale bars: 10 μm).

AlGaIn layer is also distinguished at the boundary region, energetically as well as spatially, from the other regions (*i.e.* top and side facets of the pyramid) as shown in Fig. 3c. This indicates that the Al composition of the AlGaIn layer surrounding B-QDs is lower than that of the layer surrounding P-QDs and S-QDs. Due to the lower-Al-content AlGaIn layer surrounding B-QDs, the lattice difference between the B-QDs and AlGaIn layer decreases, which leads to the reduction of the piezoelectric field of B-QDs. Consequently, the emission wavelength of B-QDs is less affected by the quantum confined Stark effect and is shorter than that of P-QDs despite occupying the same (0001) polar facet. In addition, the average height of P-QDs is higher than that of B-QDs, which also modifies the QD emission and leads to longer wavelengths in the case of P-QDs.²⁰

To clarify the relationship between the QDs and AlGaIn layers, PLE spectra were measured. In Fig. 3a, PLE spectra detected at 311 nm (blue line) and 328 nm (green line) are shown, which correspond to the emission peaks of S- and B-QDs, respectively. The PLE intensity of S-QDs dramatically decreased at ~ 275 nm (the blue arrow), which is the absorption band edge of the AlGaIn layer surrounding S-QDs. On the other hand, the PLE intensity of B-QDs decreased at ~ 287 nm (the green arrow) corresponding to the absorption band edge of the AlGaIn layer surrounding B-QDs. These PLE results are well consistent with the CL results. We emphasize that the distinct optical properties of B-QDs in relation to S- and P-QDs originated from combined differences in the surrounding AlGaIn layers and the QD average heights.

For a more detailed inspection, Fig. 4a shows the HRTEM image taken near the edge of the truncated pyramid structure.



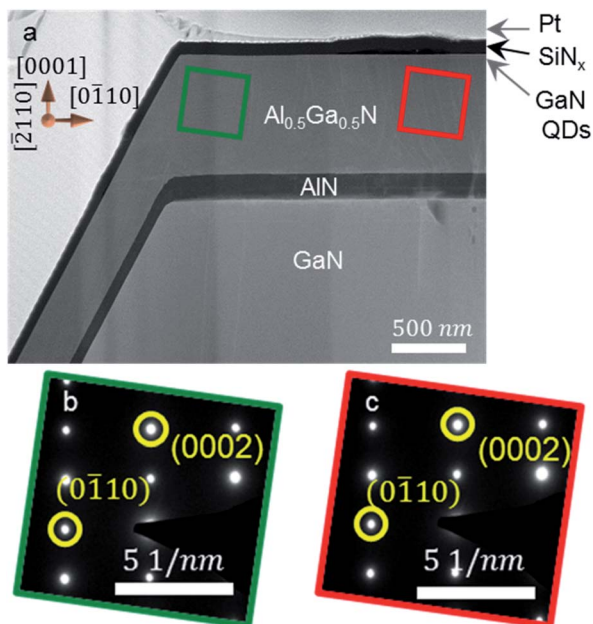


Fig. 4 (a) Cross-sectional view HAADF STEM image taken near the boundary region of the truncated pyramid structure. (b and c) SAD pattern images of the $\text{Al}_x\text{Ga}_{1-x}\text{N}$ layers below B- and P-QDs, respectively. Note that the SiN_x and Pt layers are deposited to protect the GaN QDs layers when preparing a STEM specimen.

According to a previous study,²¹ the QDs located on the boundary region of a truncated pyramid structure can release strain during the QD formation process. In this respect, the selective area diffraction (SAD) patterns of the $\text{Al}_x\text{Ga}_{1-x}\text{N}$ layers below B- and P-QDs were measured to compare the lattice difference, as shown in Fig. 4b and c, respectively. The $\text{Al}_x\text{Ga}_{1-x}\text{N}$ layer lattice distance between the two (0110) planes below B-QDs was +0.65% larger than that below P-QDs. On the other hand, along (0002) planes, the $\text{Al}_x\text{Ga}_{1-x}\text{N}$ layer lattice distance below B-QDs was -0.64% smaller than that below P-QDs. This indicates that the $\text{Al}_x\text{Ga}_{1-x}\text{N}$ layer below B-QDs was laterally stretched, which consequently reduced the lattice mismatch with B-QDs. We also investigated the strain profile of e_{yy} and e_{zz} and the result is consistent with the results obtained in a previous study²¹ (see Fig. S2†).

Furthermore, we found that the shape of B-QDs was elongated in the direction $\{10\bar{1}0\}$, unlike P-QDs, *i.e.*, the ratios between the major- and minor-axes of B- and P-QDs were 2.37 ± 1.19 and 1.29 ± 0.47 , respectively (see Fig. S1†). This result also validates that the $\text{Al}_x\text{Ga}_{1-x}\text{N}$ layer at the boundary region was laterally stretched compared to the region at the top of the pyramid, *i.e.* the boundary region had a different strain state compared to the AlGaIn region at the top of the pyramid, leading to a modification of the QD growth process and shape, as observed for the growth of GaN dots and wires on AlGaIn (1122) and (0001) surfaces.^{9,10}

Fig. 5 shows the macro-PL spectra, time-resolved PL (TRPL) results, and panchromatic CL images as a function of temperature. From the measured lifetime and PL intensity change with temperature, we could extract out the radiative and

nonradiative lifetimes as a function of temperature.²² The radiative lifetimes were 0.29, 0.35, and 0.56 ns for S-, B-, and P-QDs at 10 K, respectively. The radiative lifetime of S-QDs was faster than that of B- and P-QDs due to the negligible built-in electric field of the semipolar facet. We found that the radiative lifetime of B-QDs was faster than that of P-QDs, which also validates the reduction of the strain-induced piezoelectric field in B-QDs. With increasing temperature from 10 to 300 K, the radiative lifetimes (red lines in Fig. 5a-c) of S-, B- and P-QDs were nearly constant, indicating zero-dimensional exciton behavior.²³ On the other hand, the non-radiative process (blue lines in Fig. 5a-c) became dominant near room-temperature since thermally activated excitons can be captured by defects, because the diffusion length is long enough.²⁴

In general, the dislocation density on the *c*-plane of the truncated pyramid structure is much higher than that at a laterally over-grown semipolar facet.²⁵ With elevating temperature, however, the non-radiative lifetime of S-QDs decreased faster than the others, and was nearly comparable to the radiative lifetime above 200 K, whereas the non-radiative lifetimes of B- and P-QDs were still longer than radiative lifetimes (compare the blue and red lines in Fig. 5a-c).

To quantitatively analyze the temperature-dependent carrier behavior, we investigated the temperature-dependent PL spectra and integrated PL intensity ratio between 10 and 300 K ($I^{300\text{ K}}/I^{10\text{ K}}$) as shown in Fig. 5d. $I^{300\text{ K}}/I^{10\text{ K}}$ of the QDs is higher than that of the $\text{Al}_x\text{Ga}_{1-x}\text{N}$ matrix because the excited carriers or excitons at the $\text{Al}_x\text{Ga}_{1-x}\text{N}$ layers easily migrate into the QDs at higher temperature. However, we found that the $I^{300\text{ K}}/I^{10\text{ K}}$ of S-QDs is smaller than that of P- and B-QDs. In other words, the PL intensity of S-QDs decreased when the temperature was above 200 K, which was consistent with the fast non-radiative lifetime of S-QDs (Fig. 5a). This indicates that the thermally activated excitons of S-QDs could be delocalized and escape into the GaN wetting layer or $\text{Al}_x\text{Ga}_{1-x}\text{N}$ layers. In previous work, the QDs' height-dependent $I^{300\text{ K}}/I^{10\text{ K}}$ was investigated.²⁶ The $I^{300\text{ K}}/I^{10\text{ K}}$ of smaller height QDs (*ca.* 1 nm) was lower than that of larger height QDs (*ca.* 2.3 nm), since the small height of QDs provides a reduced carrier localization potential (and a spreading of their wave functions in the barriers), resulting in less efficient carrier confinement at higher temperatures.²⁶ In this respect, S-QDs would have weaker carrier localization than B- and P-QDs. We measured the integrated PL intensities (I) of S-, B- and P-QDs as a function of temperature (Fig. 5e), where the activation energy of QDs was estimated from an Arrhenius equation, $I = I_0(1 + A_1 e^{-E_1/K_B T} + A_2 e^{-E_2/K_B T})^{-1}$, where E_1 and E_2 are referred to as the localization energy of shallow and deep localized states, respectively. In the high temperature regime, the escape behavior of thermally activated carriers is associated with A_2 and E_2 , where A_2 describes the proportion of non-radiative recombination centers.^{27,28} The fitting parameters of A_1 , A_2 , E_1 and E_2 for S-, B- and P-QDs are listed in Table 1. Since there exists high density of threading dislocations on the (0001) polar facet propagating from the GaN template,²⁵ the proportion of non-radiative recombination centers at the polar facet can be much larger than that of the semipolar facet.²⁵ It was evident that the A_2 of P-QDs was about 10 times larger than that of S-



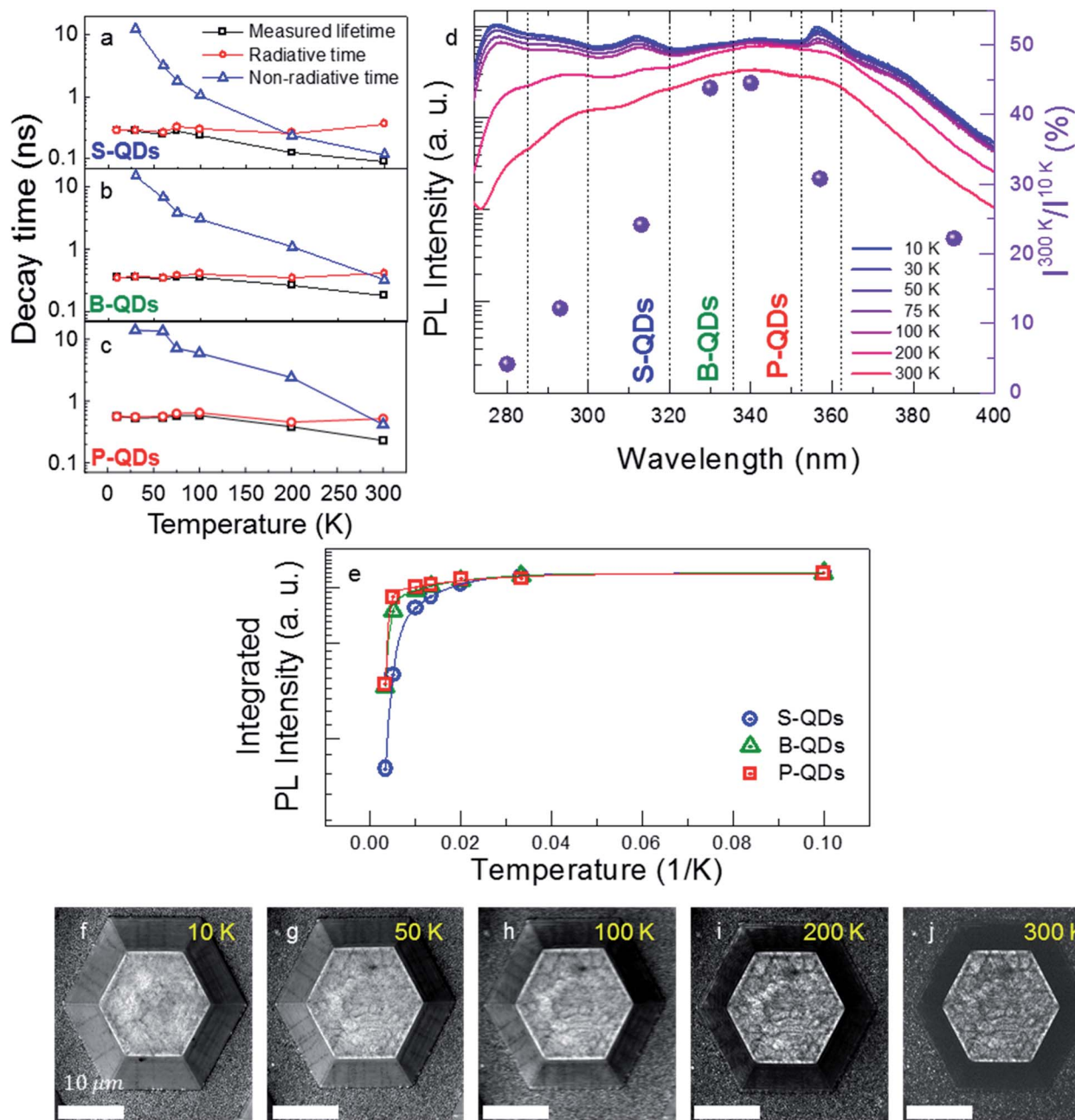


Fig. 5 (a–c) Measured, radiative and non-radiative lifetimes of S-, B- and P-QDs as a function of temperature, respectively. (d) Temperature dependent PL spectra and intensity ratio between 10 and 300 K. (e) Integrated PL intensity of S-, B- and P-QDs as a function of temperature, respectively. (f–j) Temperature dependent panchromatic CL images.

Table 1 Arrhenius equation fitting parameters for S-, B- and P-QDs

	A_1	E_1 (meV)	A_2	E_2 (meV)
S-QDs	0.92	10.43 ± 0.66	45.21	74.79 ± 2.97
B-QDs	0.32	7.62 ± 1.02	88.11	114.87 ± 8.45
P-QDs	0.19	5.51 ± 2.50	581.75	162.63 ± 43.52

QDs. For E_2 , we considered the energy difference of the valence band between the exciton transition energy of the GaN QDs and GaN wetting layer. Since the valence band offset of GaN/AlN is

about 2.45 times lower than the conduction band offset,²⁹ hole carriers would determine the activation energy for thermal escape behavior. In this respect, the energy difference of the valence band between the exciton transition energy of the GaN QDs and $\text{Al}_x\text{Ga}_{1-x}\text{N}$ layer was ~ 136 meV (~ 229 meV) for S-QDs (P-QDs). Although these values were not precisely identical to the E_2 obtained from the Arrhenius equation, this strongly indicates that the low $I^{300\text{ K}}/I^{10\text{ K}}$ of S-QDs was a result of weak carrier localization. In addition to the $\text{Al}_x\text{Ga}_{1-x}\text{N}$ layer, the thermally activated carriers could escape through the GaN wetting layer. The GaN wetting layer has a lower energy than



$\text{Al}_x\text{Ga}_{1-x}\text{N}$ layers and behaves as a GaN quantum well layer sandwiched between two $\text{Al}_x\text{Ga}_{1-x}\text{N}$ layers.^{30,31} In Fig. 5d, the emission wavelength of the GaN wetting layer is not clearly distinguishable due to our broadband UV spectrum range. To clarify the emission wavelength of the GaN wetting layer, we obtained CL spectra using local excitation (see Fig. 5f–j). When local excitation was performed on the (0001) polar facet, the emission wavelength of P-QDs was clearly distinguished from that of the GaN wetting layer and $\text{Al}_x\text{Ga}_{1-x}\text{N}$ layer, which was consistent with our previous studies.^{8,10,20} On the other hand, the emission wavelengths of S-QDs and the GaN wetting layer were found to overlap with each other, which consequently indicated a reduced band offset between S-QDs and the GaN wetting layer. As a result, the thermal escape of carriers in S-QDs was attributed to the small band offset leading to a weaker confinement compared to P-QDs and a smaller $I^{300\text{ K}}/I^{10\text{ K}}$ ratio even though the density of nonradiative recombination centers is reduced in this region.

The thermal escape behavior of carriers was also observed in the temperature-dependent panchromatic CL images, as shown in Fig. 5f–j. A homogeneous panchromatic CL intensity was observed on the whole truncated pyramid structure at 10 K, whereas the panchromatic CL intensity at the semipolar facet was relatively reduced above 200 K. We expect that maintaining the broadband UV emission spectrum at high temperature above 200 K may be possible by adjusting the QD size²⁶ and/or the surrounding AlGaIn layer with higher Al contents or by introducing QD formation without the GaN wetting layer.^{7,32} Finally, we emphasize that our unique QD combination formed on truncated pyramid structures shows great promise for solid-state based broadband UV emitters, which would not only replace conventional arc-lamps but also expand their UV applications.

Experimental section

Optical characterization

CL (monoCL4, Gatan, Inc., Pleasanton, CA, USA) equipment connected to a SEM was used, where the used acceleration voltage was 5 kV. A transmission electron microscopy specimen was prepared using a focused ion beam (Helios nanolab 450 F1). High-resolution transmission electron microscopy (HRTEM, Titan cubed G2 60-300) was employed. The elastic strain was calculated using COMSOL Multiphysics based on the theory of continuum elasticity. For the optical characterization, macro-PL, PLE and TRPL setups with a cryostat were used in the temperature range from 10 to 300 K. The macro-PL was measured with 266 nm fourth-harmonic generation of a Nd:YAG pulsed laser. The PLE was measured using xenon-lamp light dispersed by a monochromator. The TRPL was measured using 266 nm third-harmonic generation of a pulsed-mode Ti:sapphire laser and a streak camera.

Conclusions

In summary, by forming GaN QDs on GaN-based hexagonal truncated pyramid structures, we successfully demonstrated the

broadband UV emission spectrum ranging from ~ 400 nm (UV-A) to ~ 270 nm (UV-C) with homogeneous intensity. We found that the built-in electric field and growth rate were different depending on the facets of pyramid structures. As a result, the emission wavelengths for QDs grown on each facet and at the facet edges were distinct, which provides the broad UV spectrum. In particular, although B- and P-QDs were grown on the same polar facet (0001), we found that the B-QDs have distinct optical and structural properties from P-QDs, due to the locally suppressed strain in the boundary region. From temperature-dependent PL and TRPL, we found that the thermally activated excitons in S-QDs were delocalized above 200 K, as a consequence of the smaller height of S-QDs. Such behavior could be suppressed by designing suitable QD active regions with adjusted growth conditions. This work presents a solid-state based broadband UV light source that could potentially replace arc-lamp-based applications.

Conflicts of interest

There are no conflicts to declare.

Acknowledgements

This work was supported by the National Research Foundation (NRF-2019R1A2B5B03070642) of the Korea government (MSIP), and Samsung Science and Technology Foundation under Project Number SSTF-BA1602-05. J. B., S. M., B. A. and M. L. acknowledge support from the ANR Project (ANR-14-CE26-0025) “NANOGANUV”, and also from GANEX (ANR-11-LABX-0014), which belongs to the publicly funded “Investissements d’Avenir” program managed by the French ANR agency.

References

- H. Hirayama, S. Fujikawa, N. Noguchi, J. Norimatsu, T. Takano, K. Tsubaki and N. Kamata, *Phys. Status Solidi A*, 2009, **206**, 1176–1182.
- M. Kneissl, T. Kolbe, C. Chua, V. Kueller, N. Lobo, J. Stellmach, A. Knauer, H. Rodriguez, S. Einfeldt, Z. Yang, N. M. Johnson and M. Weyers, *Semicond. Sci. Technol.*, 2011, **26**, 014036.
- M. Asif Khan, *Phys. Status Solidi A*, 2006, **203**, 1764–1770.
- D. Y. Kim, J. H. Park, J. W. Lee, S. Hwang, S. J. Oh, J. Kim, C. Sone, E. F. Schubert and J. K. Kim, *Light: Sci. Appl.*, 2015, **4**, e263.
- Y.-H. Cho, H. S. Kwack, B. J. Kwon, J. Barjon, J. Brault, B. Daudin and L. S. Dang, *Appl. Phys. Lett.*, 2006, **89**, 251914.
- Y.-H. Cho, B. J. Kwon, J. Barjon, J. Brault, B. Daudin, H. Mariette and L. S. Dang, *Appl. Phys. Lett.*, 2002, **81**, 4934–4936.
- J. Brault, S. Matta, T.-H. Ngo, M. Korytov, D. Rosales, B. Damilano, M. Leroux, P. Vennéguès, M. Al Khalfioui, A. Courville, O. Totterreau, J. Massies and B. Gil, *Jpn. J. Appl. Phys.*, 2016, **55**, 05fg06.



- 8 M. Leroux, J. Brault, A. Kahouli, D. Maghraoui, B. Damilano, P. de Mierry, M. Korytov, J.-H. Kim and Y.-H. Cho, *J. Appl. Phys.*, 2014, **116**, 034308.
- 9 A. Kahouli, N. Kriouche, J. Brault, B. Damilano, P. Vennéguès, P. de Mierry, M. Leroux, A. Courville, O. Tottereau and J. Massies, *J. Appl. Phys.*, 2011, **110**, 084318.
- 10 J. Brault, T. Huault, F. Natali, B. Damilano, D. Lefebvre, M. Leroux, M. Korytov and J. Massies, *J. Appl. Phys.*, 2009, **105**, 033519.
- 11 J. Brault, S. Matta, T.-H. Ngo, D. Rosales, M. Leroux, B. Damilano, M. A. Khalifioui, F. Tendille, S. Chenot, P. De Mierry, J. Massies and B. Gil, *Mater. Sci. Semicond. Process.*, 2016, **55**, 95–101.
- 12 W. M. Hikal and B. L. Weeks, *J. Therm. Anal. Calorim.*, 2011, **110**, 955–960.
- 13 X. Zhu, K. Wang, J. Zhu and M. Koga, *J. Agric. Food Chem.*, 2001, **49**, 4790–4794.
- 14 T. Hommel and R. M. Szeimies, *Photodiagn. Photodyn. Ther.*, 2017, **17**, A14–A15.
- 15 J. Takao, K. Ariizumi, I. I. Dougherty and P. D. Cruz Jr, *Photodermatol., Photoimmunol. Photomed.*, 2002, **18**, 5–13.
- 16 M. Korytov, M. Benaissa, J. Brault, T. Huault, T. Neisius and P. Vennéguès, *Appl. Phys. Lett.*, 2009, **94**, 143105.
- 17 J.-H. Kim, B.-J. Kwon, Y.-H. Cho, T. Huault, M. Leroux and J. Brault, *Appl. Phys. Lett.*, 2010, **97**, 061905.
- 18 S.-H. Lim, Y.-H. Ko, C. Rodriguez, S.-H. Gong and Y.-H. Cho, *Light: Sci. Appl.*, 2016, **5**, e16030.
- 19 T. Huault, J. Brault, F. Natali, B. Damilano, D. Lefebvre, L. Nguyen, M. Leroux and J. Massies, *Appl. Phys. Lett.*, 2008, **92**, 051911.
- 20 S. Matta, J. Brault, T. H. Ngo, B. Damilano, M. Korytov, P. Vennéguès, M. Nemoz, J. Massies, M. Leroux and B. Gil, *J. Appl. Phys.*, 2017, **122**, 085706.
- 21 S. Zhou, Y. Liu, D. Wang, Z. Yu, W. Zhao, L. Le and P. O. Holtz, *Superlattices Microstruct.*, 2015, **84**, 72–79.
- 22 J.-H. Kim, Y.-H. Ko, J.-H. Cho, S.-H. Gong, S.-M. Ko and Y.-H. Cho, *Nanoscale*, 2014, **6**, 14213–14220.
- 23 Y. H. Ko, J. H. Kim, L. H. Jin, S. M. Ko, B. J. Kwon, J. Kim, T. Kim and Y. H. Cho, *Adv. Mater.*, 2011, **23**, 5364–5369.
- 24 M. Kim, S. Choi, J. H. Lee, C. Park, T. H. Chung, J. H. Baek and Y. H. Cho, *Sci. Rep.*, 2017, **7**, 42221.
- 25 D. Zhu, D. J. Wallis and C. J. Humphreys, *Rep. Prog. Phys.*, 2013, **76**, 106501.
- 26 J. Brault, D. Rosales, B. Damilano, M. Leroux, A. Courville, M. Korytov, S. Chenot, P. Vennéguès, B. Vinter, P. De Mierry, A. Kahouli, J. Massies, T. Bretagnon and B. Gil, *Semicond. Sci. Technol.*, 2014, **29**, 084001.
- 27 Y. Sun, Y.-H. Cho, H. M. Kim, T. W. Kang, S. Y. Kwon and E. Yoon, *J. Appl. Phys.*, 2006, **100**, 043520.
- 28 Y.-H. Ko, J.-H. Kim, S.-H. Gong, J. Kim, T. Kim and Y.-H. Cho, *ACS Photonics*, 2015, **2**, 515–520.
- 29 S. H. Wei and A. Zunger, *Appl. Phys. Lett.*, 1996, **69**, 2719–2721.
- 30 W. Yang, R. R. Lowe-Webb, H. Lee and P. C. Sercel, *Phys. Rev. B: Condens. Matter Mater. Phys.*, 1997, **56**, 13314–13320.
- 31 C. Lobo, R. Leon, S. Marcinkevicius, W. Yang, P. C. Sercel, J. Zou, X. Z. Liao and D. J. H. Cockayne, *Phys. Rev. B: Condens. Matter Mater. Phys.*, 1999, **60**, 16647–16651.
- 32 P. B. Joyce, T. J. Krzyzewski, G. R. Bell, B. A. Joyce and T. S. Jones, *Phys. Rev. B: Condens. Matter Mater. Phys.*, 1998, R15981–R15984.

